


Article

Low Temperature Synthesis of Photocatalytic Mesoporous TiO₂ Nanomaterials

Massimo Dell'Edera ^{1,2}, Francesca Petronella ^{1,†} , Alessandra Truppi ^{1,‡},
Leonarda Francesca Liotta ³ , Nunzio Galli ³, Teresa Sibillano ⁴, Cinzia Giannini ⁴ ,
Rosaria Brescia ⁵, Francesco Milano ⁶ , Marinella Striccoli ¹ , Angela Agostiano ^{1,2} ,
Maria Lucia Curri ^{1,2,*} and Roberto Comparelli ^{1,*} 

¹ CNR-IPCF, Istituto per i Processi Chimico-Fisici, S.S. Bari, c/o Dip. Chimica Via Orabona 4, 70126 Bari, Italy; m.delledera@ba.ipcf.cnr.it (M.D.); f.petronella@ba.ipcf.cnr.it (F.P.); a.truppi@ba.ipcf.cnr.it (A.T.); m.striccoli@ba.ipcf.cnr.it (M.S.); angela.agostiano@uniba.it (A.A.)

² Università degli Studi di Bari Aldo Moro, Dip. Chimica, Via Orabona 4, 70126 Bari, Italy

³ Istituto per lo Studio dei Materiali Nanostrutturati (ISMN)-CNR, via Ugo La Malfa, 153, 90146 Palermo, Italy; leonardafrancesca.liotta@cnr.it (L.F.L.); nunzio.galli@cnr.it (N.G.)

⁴ CNR-IC, Istituto di Cristallografia, Via Amendola 122/O, 70126 Bari, Italy; teresa.sibillano@ic.cnr.it (T.S.); cinzia.giannini@ic.cnr.it (C.G.)

⁵ Electron Microscopy Facility, Istituto Italiano di Tecnologia (IIT), via Morego 30, 16163 Genova, Italy; Rosaria.Brescia@iit.it

⁶ CNR-ISPAA Istituto di Scienze delle Produzioni Alimentari, Consiglio Nazionale delle Ricerche, S.P. Lecce-Monteroni, 73100 Lecce, Italy; f.milano@ba.ipcf.cnr.it

* Correspondence: lucia.curri@ba.ipcf.cnr.it (M.L.C.); roberto.comparelli@cnr.it (R.C.)

† Present address: CNR—IC, Istituto di Cristallografia, S.S. Roma, Via Salaria Km 29,300, 00015 Monterotondo—Rome, Italy.

‡ Present address: TCT—Nanotech Division, TCT s.r.l. Strada per Pandi, 3 72100 Brindisi, Italy.

Received: 30 June 2020; Accepted: 4 August 2020; Published: 7 August 2020



Abstract: We report the synthesis of mesoporous TiO₂ nanostructures based on the decomposition of TiOSO₄ in aqueous alkaline solution at room temperature, followed by mild thermal treatment (110 °C) in an oven and suitable to yield up to 40 g of product per batch. The duration of the thermal treatment was found to be crucial to control crystalline phase composition, specific surface area, surface chemistry and, accordingly, the photocatalytic properties of the obtained TiO₂ nanocrystals. The thorough investigation of the prepared samples allowed us to explain the relationship between the structure of the obtained nanoparticles and their photocatalytic behavior, that was tested in a model reaction. In addition, the advantage of the mild treatment against a harsher calcination at 450 °C was illustrated. The proposed approach represents a facile and sustainable route to promptly access an effective photocatalyst, thus holding a significant promise for the development of solutions suitable to real technological application in environmental depollution.

Keywords: titanium dioxide; photocatalysis; nanoparticles; mesoporous

1. Introduction

In recent years, an enormous research effort of scientific community has been focusing towards novel technologies for environmental remediation. Among the most critical environmental issues, the exponential increase in pollutants in wastewater has urged particular attention, as several studies have confirmed the presence in water bodies of emerging pollutants [1], that are a class of compounds, including pharmaceutical and personal care products or pollutants coming from civil, industrial and agricultural waste sewage, and have a tremendous environmental impact, and thus represent a

critical issue for the conventional pollution remediation methods. Therefore, increasing attention has been focused on a class of water treatment processes called “Advanced Oxidation Processes” [2], which represent very appealing strategies. In particular, among such strategies, very relevant are photocatalytic processes based on the use of semiconductor materials that, upon UV irradiation, are able to assist in the degradation of different classes of organic compounds, including the emerging pollutant molecules, without using any other chemicals. The most investigated semiconductor material for environmental clean-up applications is TiO_2 , due to its excellent photocatalytic performance [3–6]. TiO_2 shows high photoactivity, high chemical and photochemical stability, high oxidative efficiency and low production cost. In particular, nanosized TiO_2 demonstrated improved performances with respect to its bulk counterpart thanks to its extremely high surface-to-volume ratio, which can greatly increase the density of active sites available for adsorption and catalysis. Many strategies have been reported for obtaining TiO_2 nanoparticles (NPs) [7], including sol gel, hydrothermal and solvothermal methods, chemical vapor deposition [8]. The final properties of the synthesized NPs depend on synthetic technique, precursors composition and reaction conditions [9–11]. In particular, the photoactivity of TiO_2 NPs is strongly dependent on its crystalline phase. Indeed, the anatase phase has been generally regarded as the most photoactive crystalline phase of TiO_2 [12,13]; however, several examples of increased photoactivity due to a mix of different crystalline phases have been reported [14,15]. The concomitant presence of different crystalline phases can be seen as being beneficial to improve the photocatalytic efficiency of the TiO_2 , as a suitable combination of crystalline phases, with an appropriate alignment of the conduction and valence band edge positions, enable a charge transfer between the different phase domains, thus limiting the detrimental recombination phenomena of electrons and holes [16–18]. Most of the reported synthetic approaches needs high reaction temperatures and/or single or multiple post-synthesis calcination steps at a temperature higher than 300 °C to promote crystallization in anatase phase [19–21]. However, a post-synthesis calcination process is likely to lead to an extensive sintering of the NPs, turning into an overall reshaping of the obtained structures, a loss of specific surface area and decrease in the porosity of the final material [22]. Remarkably, such textural properties, i.e., porosity and surface area, play an important role in determining the photocatalytic performances of the catalysts. Indeed, mesoporous TiO_2 —that, is a TiO_2 -based material featuring either in-particle and interparticle pores, with diameters between 2 and 50 nm—is currently regarded as promising material for photocatalytic applications, since the high porosity is expected to improve the photocatalytic performances, so as to compensate for the NC aggregation phenomena occurring due to the post-synthetic thermal treatment [8]. Moreover, another challenge for a technologically viable synthetic approach, able to provide TiO_2 NPs with an adequate morphological and structural control, is represented by the reaction yield. Indeed, the lack of scalable and cost effective synthetic routes has so far significantly hampered the large scale application of the nanosized photocatalysts for environmental purposes [23]. Therefore, the present work aims at investigating a new, potentially scalable, route for the low-temperature synthesis of TiO_2 nanostructures, anatase in phase, with high surface area or mesoporous structure.

In particular, we report the gram scale synthesis of mesoporous TiO_2 based on the decomposition of TiOSO_4 in aqueous alkaline solution at room temperature. The obtained “as prepared” TiO_2 is shown to be formed of very small nanocrystals (approximately 1 nm), brookite in nature, and presents a high surface area (over 503 m^2/g) and a mesoporous structure. However, the prepared nanomaterial shows a very limited photocatalytic performance when tested in photocatalytic experiment. Interestingly a mild thermal treatment, at 110 °C, on the prepared TiO_2 is found to promote a progressive transition of the pristine brookite phase toward the anatase crystalline structure, as a function of the duration of the thermal treatment (in the range between 2 and 24 h). Importantly, the proposed synthesis protocol does not require any organic molecule as a porogenic agent, therefore the high-cost calcination step, often mandatory to remove the organic porogenic agent, is purposely avoided and replaced by the mild thermal treatment that promotes a conversion from brookite to anatase, without drastically undermining the textural features. The photocatalytic performance of the TiO_2 nanostructures has been

assessed in the degradation of the model molecule, methylene blue (MB), showing a progressive increase (up to 1.5 times) for the photocatalyst obtained after prolonged thermal treatment. The overall results indicate that the proposed synthesis represent a viable, easily up-scalable and sustainable approach to achieve a photocatalytically active mesoporous TiO_2 , characterized by a relevant technological potential that holds a great promise for real application in the field of environmental depollution.

2. Results and Discussion

The synthesis of TiO_2 nanoparticles (NPs) involves TiOSO_4 as cost effective Ti^{4+} precursor, and exploits a precipitation method in alkaline solution by dropwise addition of the TiOSO_4 solution to NH_4HCO_3 (Figure 1A) under constant magnetic stirring. Upon mixing, TiOSO_4 suddenly reacts, promoting the formation and precipitation of Ti-hydroxide species, resulting in a coalescence of the reaction mixture that turns into a milky slurry at the end of the reaction. The obtained nanocrystals were collected by centrifugation at 3000 rpm and the precipitate was repeatedly washed by subsequent cycles of dispersion in water and centrifugation. At this stage, the obtained white precipitate was thermally treated in an oven at 110 °C for 2, 8, 16 and 24 h, respectively. The obtained samples were comprehensively investigated by integrating a number of complementary techniques, namely DRS (Diffuse Reflectance Spectroscopy), TGA/DTA (Thermogravimetric Analysis/Differential Thermal Analysis), N_2 adsorption-desorption isotherms, HRTEM (high-resolution transmission electron microscopy), STEM/EDS (scanning transmission electron microscopy/energy dispersive spectroscopy), SEM (scanning electron microscopy), XRD (X-ray diffraction) and finally, their photocatalytic activity was evaluated spectrophotometrically, by monitoring photocatalyst-assisted decoloration of a dye molecule, methylene blue, selected as a model compound.

All the investigated TiO_2 samples show the typical absorbance onset at 345 nm, irrespective of the duration of the thermal treatment, corresponding to a band gap of 3.65 eV, calculated according to the Tauc plot [24]. The DR spectrum of a representative sample (TiO_2 _16 h) is reported in Figure 1B.

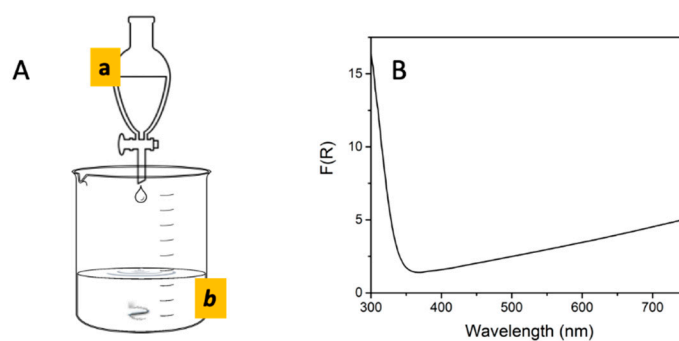


Figure 1. (A) Schematic representation of the synthetic set up: (a) dropping funnel containing the TiOSO_4 0.64 M water solution dripping in (b) NH_4HCO_3 2 M water solution. (B) DR spectrum reported as a Kubelka-Munk function ($F(R)$) of a representative TiO_2 sample (TiO_2 _16 h) deposited onto quartz slides.

Table 1 and Figure 2 and Figure S1 report the main results of the structural characterization performed by means of XRD analysis on TiO_2 NPs samples as a function of the thermal treatment duration at 110 °C. Surprisingly, after the purification step, the TiO_2 sample (TiO_2 _0 h) shows an initial crystalline structure characterized by a dominant presence of brookite (85%) and a reduced amount of anatase (15%). After 2 h of thermal treatment, the two polymorphs occur almost in the same percentage (53% anatase and 47% brookite). For a longer treatment time, the phase composition of the samples changes significantly, with anatase becoming the prevalent phase. Indeed, between 8 and 16 h of treatment, the TiO_2 sample is shown to be composed of 75% anatase phase, and 25% brookite phase. Finally, after 24 h of thermal treatment, anatase and brookite appear in the percentages of 81% and 19%, respectively. In summary, immediately after the precipitation reaction, the dominant crystallographic

phase in the TiO₂ NPs is brookite, and as thermal treatment proceeds, the brookite phase progressively converts into the anatase phase, as depicted in Figure 3.

Table 1. Crystallographic composition of the TiO₂ NPs as a function of the duration of the thermal treatment.

Sample	Anatase Phase	Brookite Phase
TiO ₂ _0 h	15% ± 5%	85% ± 5%
TiO ₂ _2 h	53% ± 3%	47% ± 3%
TiO ₂ _8 h	75% ± 3%	25% ± 3%
TiO ₂ _16 h	74% ± 3%	26% ± 3%
TiO ₂ _24 h	81% ± 3%	19% ± 3%

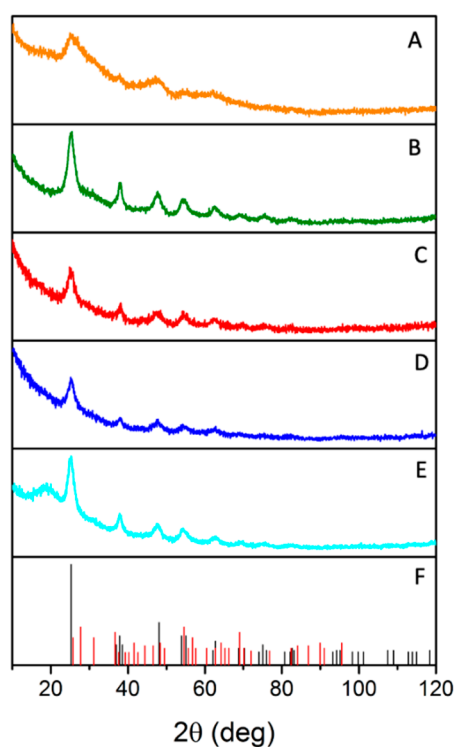


Figure 2. XRD experimental patterns of as prepared TiO₂ nanoparticles (NPs) before (A), and after the thermal treatment in an oven at 110 °C for 2 h ((B), TiO₂_2 h), 8 h ((C), TiO₂_8 h), 16 h ((D), TiO₂_16 h) and 24 h ((E), TiO₂_24 h). Bragg hkl reflections positions for anatase phase (black line, panel (F)) and brookite phase (red line, panel (F)) respectively, are reported.

The XRD patterns were also analyzed by a whole-profile Rietveld-based fitting program according to a procedure fully described elsewhere [25]: the fitting procedure carried out the XRD patterns including only the TiO₂ anatase phase, which allows us to evaluate the coherent crystal apparent domain size which remains substantially constant (around 3.3 nm ± 0.5) all along the thermal treatment duration.

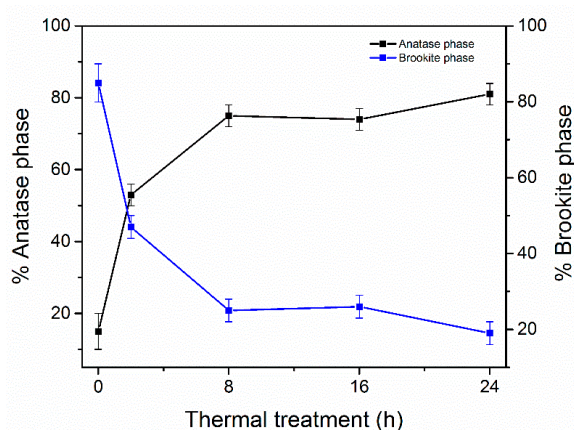


Figure 3. Percentage of anatase and brookite in the prepared samples estimated by quantitative phase analysis of XRD patterns as a function of thermal treatment duration in an oven at 110 °C.

The bright field TEM (BF-TEM) micrographs of TiO₂ NCs before and after thermal treatment at 110 °C in an oven are reported in Figure 4. The variation of NP morphology and size can be put in correlation with thermal treatment duration. Indeed, the as prepared TiO₂ NPs are very small (approximately 1 nm in diameter) with irregular shape. The thermal treatment promotes an increase in NP size (Table 2) and a reshaping towards spherical-like NPs. In fact, the samples TiO₂_2 h and TiO₂_8 h (Figure 4B,C, respectively) are characterized by slightly larger particles (4 ± 1 and 13 ± 8 nm, respectively). After 16 h of thermal treatment (Figure 4D), even larger particles are visible, and spherical in shape (diameter 23 ± 6 nm; Table 2). A prolonged thermal treatment, up to 24 h (Figure 4E), does not results in any substantial modification of the NP morphology (still spherical particles are observed) and size (diameter 22 ± 7 nm). A representative SEM micrograph of the TiO₂_16 h sample (Figure 4F) shows that the sample is composed of micrometric aggregates of NPs irrespective of thermal treatment duration (data not reported).

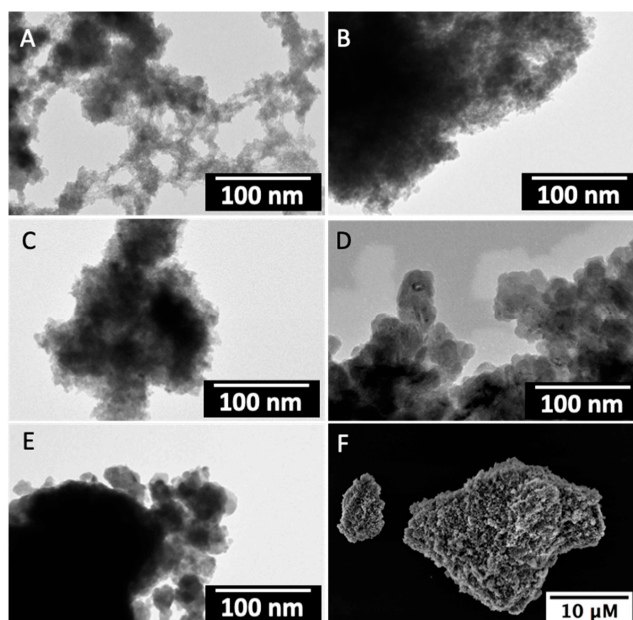


Figure 4. TEM micrographs of synthesized TiO₂ NPs before ((A), TiO₂_0 h) and after the thermal treatment at 110 °C in an oven carried out for 2 h ((B), TiO₂_2 h), 8 h ((C), TiO₂_8 h), 16 h ((D) TiO₂_16 h) and 24 h ((E), TiO₂_24 h). SEM micrograph of TiO₂ NCs aggregates after 16 h of thermal treatment at 110 °C in oven (F).

Table 2. Statistical evaluation of TiO₂ NPs size after the thermal treatment at 110 °C in oven carried out for 2 h (TiO₂_2 h), 8 h (TiO₂_8 h), 16 h (TiO₂_16 h) and 24 h (TiO₂_24 h). At least 100 NPs were measured for each sample.

Sample Name	Size (nm)
TiO ₂ _0 h	~1
TiO ₂ _2 h	4 ± 1
TiO ₂ _8 h	13 ± 8
TiO ₂ _16 h	23 ± 6
TiO ₂ _24 h	22 ± 7

BF-TEM images of TiO₂_16 h clearly show that the samples are composed by aggregates, formed of few nm sized, single-crystal particles, as can be observed by HRTEM.

HRTEM analyses do not allow to us distinguish between the anatase and brookite phases, due to both the inherent accuracy of magnification calibration in HRTEM, not higher than 5% [26], and the similarity of the two polymorphs of TiO₂, that share the octahedral coordination of Ti atoms but slightly differ in the way the TiO₆ octahedra are linked [27]. For this reason, the indexing of the fast Fourier transforms (FFTs) of HRTEM images in Figure 5 is done based on both phases.

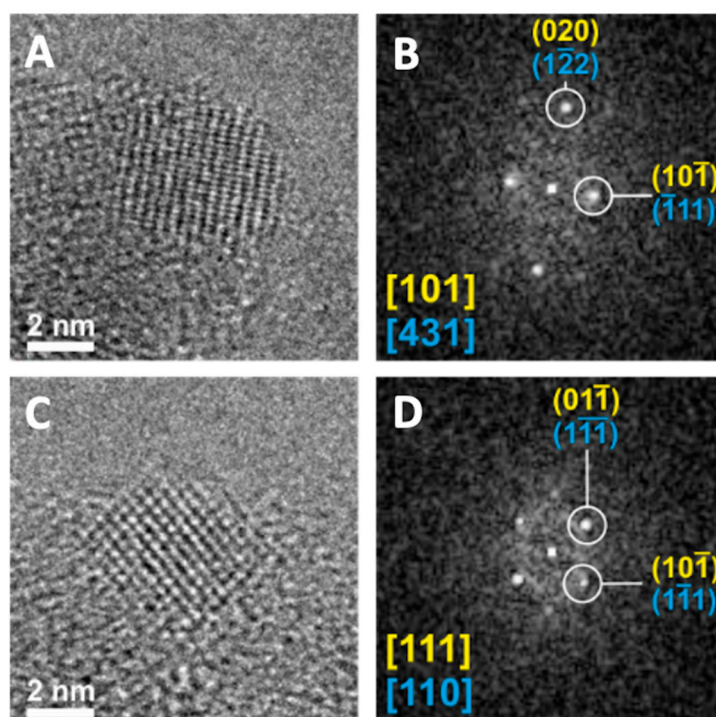


Figure 5. HRTEM: Crystal structure analysis of individual TiO₂ NPs in the aggregates. (A,C) HRTEM images and (B,D) respective fast Fourier transforms (FFTs) of zone-axis oriented selected particles. The observed structures can be attributed to anatase (yellow annotations) or to brookite (cyan annotations).

The occurrence of brookite as the prevalent phase immediately after the purification step can be ascribed to a high stoichiometric excess of bicarbonate and carbonate anions present in the reaction medium with respect to the TiO₂ precursor (approximately 5:1 according to the investigated experimental condition). Under these conditions, bicarbonate and carbonated anions, similarly to oxalate anions, can act as rigid bidentate ligands [26,27], able to bridge two Ti centers, thus leading to a chelate complex that promotes the stabilization of the oxide, namely the metastable brookite phase, as previously reported [28]. Several reports, indeed, indicated that brookite generation takes place through the formation of water-soluble titanium complexes including oxalates [28], citrates [29] and

lactates [30]. The small fraction of anatase phase present in the investigated as-prepared sample can be associated to the presence of sulphate anions. The dropwise addition of the acidic TiOSO_4 solution to the NH_4HCO_3 solution determines a progressive decrease in the pH of the resulting mixed solution and a concomitant generation of the zero-charge complex $[\text{Ti}(\text{OH})_4(\text{H}_2\text{O})_2]^0$. The complexes can condense due to ololation and oxolation reactions, thus resulting in the formation of crystallization nuclei and their subsequent growth. Remarkably, in the presence of sulphate anions, the condensation reaction promotes the generation of anatase structure, since sulphate anions, entering in the coordination sphere of Ti, behave as structure directing agents, as previously demonstrated [28]. Under the investigated experimental conditions, the conversion of the chelate complex of Ti with carbonate/bicarbonate species in brookite, along with the concomitant generation of anatase phase through the condensation reaction of Ti complexes, can be further promoted by mild heating, in agreement with previous reports [31–34]. Indeed, a progressive conversion of brookite into anatase as a function of thermal treatment duration can be observed in Figure 3. Such evidence seems rather surprising, as brookite is generally recognized as more thermodynamically stable than anatase [35,36]. However, the thermodynamic stability, and, accordingly, the phase conversion process may be affected by the initial size of the nanocrystals. In fact, for nanocrystals up to 11 nm in size, anatase is reported to be the most stable phase, while brookite becomes the most stable phase for size between 11 and 35 nm [37]. In our experiments, the initial crystallite size is below 11 nm, therefore, as calculated by Zhang and Banfiel [38], the formation enthalpy of brookite is higher than that of anatase. Accordingly, it can be reasonably thought that, during the thermal treatment, the less stable brookite particles are progressively converted in the more stable anatase NPs, with the brookite to anatase transformation being energetically downhill.

In Figure 6A, the TGA curves registered as a function of time and temperature for the sample TiO_2 _0 h treated at 110 °C under air flow for 2 and 8 h, respectively, are reported. This conversion from brookite to the anatase phase starts to appear already after 2 h treatment, getting to completion after 8 h. The corresponding DTA profiles as a function of time are shown in Figure 6B. TGA/DSC experiments were carried out to elucidate the effect of the thermal treatment performed on the TiO_2 samples, in order to investigate the weight loss and the enthalpic balance of the processes that take place during the thermal cycle. When the temperature is increased from 25 to 110 °C, a rapid weight loss, from 100% to 87%, is observed in the first 0.1 h at 107 °C and subsequently to 85% after 0.2 h, when a temperature of 110 °C is reached (see Figure 6A,C where the modifications occurring during the first 0.5 h are displayed). Afterwards only a slight decrease in weight is detected, to 83.2 and to 82.45 wt%, after 2 and 8 h of treatment at 110 °C, respectively. Interestingly, the observed weight losses are concomitant with the changes observed in the crystalline phase composition of the sample, that, starting from an initial composition characterized by a prevalence of brookite (85%) in the as prepared sample, ends up with a dominant anatase phase (75%) after 8 h of thermal treatment (Table 1).

The DTA curves (Figure 6B,D) show an endothermic peak, likely due to water loss, appearing during the first 0.1–0.15 h, then, no other significant heat changes are detected, until the end of the experiment.

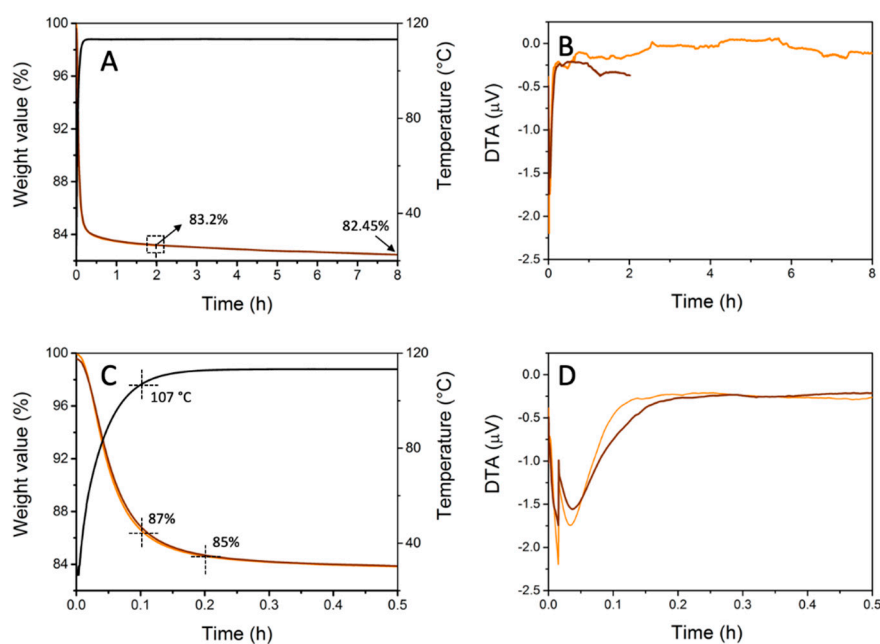


Figure 6. TGA (panel (A,C)) and DTA (panel (B,D)) curves registered versus temperature up to 110 °C (black line) and time 2 h (orange line), 8 h (brown line) registered for the sample TiO₂_0 h treated under air flow.

Figure 7A displays the N₂ adsorption/desorption isotherms that are of type IV for all TiO₂ NP samples. A very reduced hysteresis loop (H3 or H4 type) is just visible between 0.4 and 0.6 p/p⁰ only for TiO₂ 0 and TiO₂ 2 h and then at relatively high pressure, ~0.9–1.0 p/p⁰, for all samples. According to the relevant literature [39], such types of hysteresis are usually found in solids forming a slit-shaped porous network with non-uniform (H3 type) or uniform (H4 type) size. By increasing the temperature and duration time of the treatment, the isotherm curves, as well the hysteresis loop, become gradually flatter according to a decrease in specific surface area (SSA) and porosity, as a consequence of the particle growth and the inter-particles void drop. The textural parameters derived from N₂ physisorption experiments are listed in Tables 3 and 4. The average pore distribution is centered between 3 and 4 nm when the Barrett-Joyner-Halenda (BJH) model is applied and comparable values for the pore diameters were obtained from both adsorption and desorption branches, suggesting the presence of cylindrical pores and/or of interparticles voids with uniform size. In Figure 7B, the pore size distribution as dV/dW (cm³/g*nm) vs. pore width (nm) calculated by the Barrett-Joyner-Halenda (BJH) model applied to the desorption curve is shown.

In Figure 8, the cumulative pore volume (cm³/g) vs. the pore width (nm) is displayed and the slope of the curves confirms how the duration of the treatment affects the properties of the TiO₂ samples.

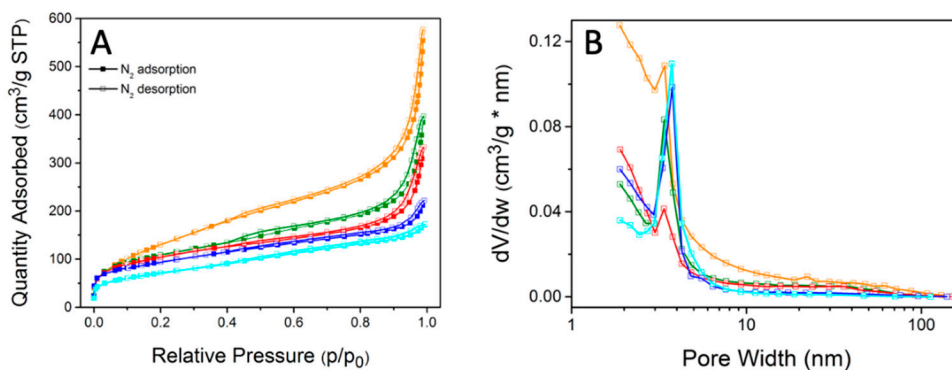


Figure 7. (A) N_2 adsorption/desorption isotherms registered for the TiO_2 NP samples as a function of temperature and duration time of the treatment. All the curves (type IV) are characteristic of mesoporous solids with H1-type hysteresis [37]. (B) Pore size distribution as dV/dw ($cm^3/g \cdot nm$) vs. pore width (nm) calculated by the Barrett-Joyner-Halenda (BJH) model on the desorption branch of isotherms for TiO_2 samples. TiO_2 samples are reported using following color code: TiO_2 _0 h (orange line), TiO_2 _2 h (green line), TiO_2 _8 h (red line), TiO_2 _16 h (blue line), TiO_2 _24 h (light blue line).

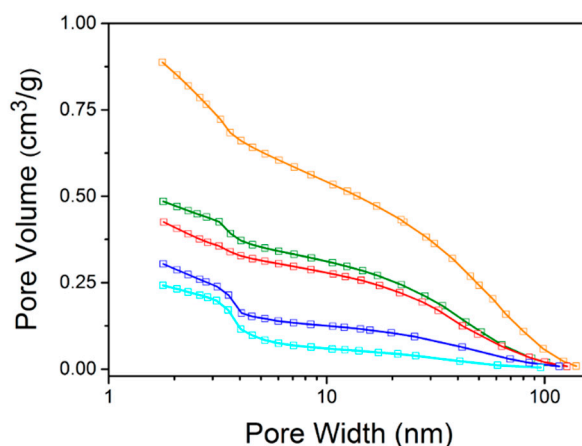


Figure 8. Cumulative pore volume (cm^3/g) vs. pore width (nm) calculated by BJH model on the desorption branch of isotherms for different TiO_2 samples: TiO_2 _0 h (orange line), TiO_2 _2 h (green line), TiO_2 _8 h (red line), TiO_2 _16 h (blue line), TiO_2 _24 h (light blue line).

Furthermore, as listed in Table 3, the average sizes of TiO_2 particles or agglomerates of crystallites were calculated by means of BET analysis (d_{BET}) using the following equation: $d_{BET} = n/\rho \times SSA$, where ρ is the theoretical density of anatase (3.90 g/cm^3), SSA is the specific surface area (m^2/g) of the TiO_2 samples determined by BET measurement and n is the shape factor of the particle, being equal to 6 for a sphere. Such an equation is based on a simplified model, i.e., the surface area of a sample is the sum of the surface of each particle in the sample. Since d_{BET} values agree well with the crystallite size calculated by XRD, it can be inferred that each crystallite in the sample, though assembling in a larger structure and getting in contact with each other, preserve its own individuality, as also confirmed by TEM analysis. The empty space between the aggregate of nearly spherical NPs gives rise to a porous structure due to the occurrence of interparticle voids and the evolution of the resulting texture is clearly pointed out by the results of the BET analysis of the samples. This assumption is consistent with the formation of a mesoporous material [8,40,41], occurring here without any porogenic compound—surfactant molecule—that behave as soft templating agent, able to induce pore formation, that would have, in fact, required a high temperature thermal treatment or, as an alternative, a series of washing steps with strong acid solution. Indeed, the proposed mild thermal treatment, while promoting the anatase phase formation, is suited to prevent the nanocrystals from turning into a more compact material, which is, instead, typical of the much harsher calcination procedure.

Table 3. Specific surface area (SSA) (by BET method) and porosity values of TiO₂ samples.

Sample	SSA (m ² /g)	d _{BET} (nm)	BJH Adsorption Average Pore Width (nm)	BJH Desorption Average Pore Width (nm)	BJH Cumulative Pore Volume * (cm ³ /g)
TiO ₂ _0 h	503.0	3.0	3.38	3.40	0.887
TiO ₂ _2 h	354.0	4.35	3.38	3.41	0.485
TiO ₂ _8 h	350.0	4.39	3.49	3.50	0.425
TiO ₂ _16 h	336.5	4.57	3.68	3.70	0.304
TiO ₂ _24 h	255.7	6.0	3.69	3.71	0.232

* The BJH cumulative pore volume was calculated from the desorption branch.

In order to get a more comprehensive description of the pore size distribution and shape, pore width values were also calculated by the Gurvitsch method, according to the equation ($4V/A$), where V is the total pore volume at p/p_0 0.98 and A is the BET surface area (see Table 4). According to the relevant literature [42], the BJH method, usually valid for calculating the pore width of cylinders, slits and voids between solid spherical NPs, however, may underestimate in some cases (e.g., gel materials) the size of pores, because it neglects the effect of the curvature of the pore walls on the thickness of the adsorbed gas layer. On the other hand, the Gurvitsch method ($4V/A$) works well for determining the pore sizes of mesoporous materials with cylindrical pores that have a narrow size distribution [42]. In order to compare the pore—or the intraparticle void—size in the TiO₂ samples, values derived from the BJH and Gurvitsch methods were compared (see Tables 3 and 4).

It is shown that Gurvitsch pore size values are higher than the BJH values found for TiO₂ samples treated for 0.2 and 8 h, respectively, while comparable values were obtained from the two methods for longer thermal treatments, 16 and 24 h. T.

Such a result is consistent with the formation, upon thermal treatment of a stable porous structure where the effect of the curvature of the pore walls upon the thickness of the adsorbed gas layer becomes negligible. Finally, the contribution of micropores to the texture of the TiO₂ samples was evaluated by applying the Horvath-Kavazoe method [43].

Table 4. Porosity values of TiO₂ samples calculated by the Gurvitsch ($4V/A$) and by Horvath-Kavazoe methods.

Sample	Total Pore Volume (cm ³ /g) at p/p_0 0.98	Gurvitsch Pore Width (nm)	Horvath-Kavazoe Micropore Width (nm)	Horvath-Kavazoe Micropore Volume (cm ³ /g) at p/p_0 0.16
TiO ₂ _0 h	0.926	7.3	0.81	0.19
TiO ₂ _2 h	0.487	5.5	0.65	0.16
TiO ₂ _8 h	0.431	4.9	0.62	0.14
TiO ₂ _16 h	0.308	3.6	0.61	0.13
TiO ₂ _24 h	0.235	3.7	0.60	0.11

On the basis of values listed in Tables 3 and 4, irrespective of the applied model, all the results point to a decrease in surface area and porosity (in terms of interparticle pores or voids, micropores and related pores volume) by increasing the temperature and the duration of treatment. In particular, the main changes in the morphological properties occur at first by increasing the drying temperature from 50 to 110 °C, namely by comparing TiO₂_0 h and TiO₂_2 h (TiO₂_2 h behaves similarly to TiO₂_8 h), and then increasing the duration of 110 °C treatment from 8 to 16 h. In fact, TiO₂_16 h \cong TiO₂_24 h.

In Figure 9, the results of photocatalytic experiments are reported. Since, to best of our knowledge, a standard method for the characterization of photocatalytic efficiency of TiO₂ nanocatalysts in the form of a powder sample is not available, a test was set up on the basis of the conditions reported for the ISO standard 10678 (2010), that has been established for the determination of photocatalytic activity of surfaces in an aqueous medium by degradation of MB. Indeed, the photocatalytic performance of the prepared TiO₂ NP samples was tested by using a light flux of 0.2 mW/cm, a 10⁻⁵ M MB aqueous solution, at pH 6, just in agreement with the ISO standard conditions. In addition, the photocatalytic experiment was performed by using an irradiation source at 254 nm, keeping the solution under

constant magnetic stirring, which has been identified as more suited to the peculiar characteristics of the catalysts under investigation, presenting an absorption onset at 345 nm and precipitating from the water dispersion if not properly stirred. Moreover, a standard conditioning time of 30 min in the dark was applied for all samples to achieve a reliable adsorption–desorption equilibrium of MB at the surface of the catalysts.

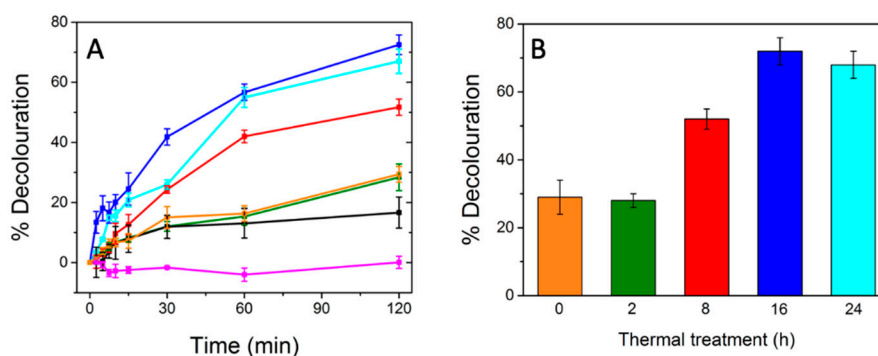


Figure 9. Panel (A) Time course evolution of methylene blue (MB) decoloration at pH 6, under UV irradiation, assisted by TiO₂_0 h (orange line), TiO₂_2 h (green line), TiO₂_8 h (red line), TiO₂_16 h (blue line), TiO₂_24 h (light blue line). Experiments were evaluated by monitoring the MB absorbance intensity at 664 nm. Control experiments in absence of photocatalyst (violet line) and at dark (black line) are reported. Experimental data are presented as mean values \pm standard deviation obtained from the analysis of five replicates. Panel (B) Histogram chart showing the percentage of MB decoloration after 120 min of UV irradiation at pH 6 as a function of thermal treatment time the TiO₂ NPs. MB concentration: 1×10^{-5} M. Experimental data are presented as mean values \pm standard deviation obtained from the analysis of five replicates.

In Figure 9, the time course evolution of the MB decoloration assisted by the TiO₂ NP samples obtained for increasing thermal treatment duration (panel A) is reported, while in panel B, the histogram showing the percentage of MB decoloration after 120 min of UV irradiation as a function of thermal treatment time is displayed. Negligible degradation is observed in the absence of a catalyst. For all samples, the adsorption of MB was also investigated, and the adsorption measured for all the investigated samples is of ca. $(17 \pm 5)\%$ after 120 min. The reported data clearly highlight that the prepared TiO₂ NPs are photoactive already before any thermal treatment, although with a not exceedingly high decoloration value, $(29 \pm 5)\%$. The photocatalytic performance does not significantly improve for the sample thermally treated for 2 h (TiO₂_2 h) $(28 \pm 4)\%$. The TiO₂_8 h sample shows an enhancement of the photocatalytic performance, with $(52 \pm 3)\%$ of decoloration. A further increase in the duration of the thermal treatment systematically results in an increase in the photocatalytically assisted decoloration, up to $(72 \pm 4)\%$ for the TiO₂_16 h sample. Finally, for the TiO₂_24 h sample, no significant difference in the extent of the decoloration $((68 \pm 5)\%)$ is observed, being, in fact the difference within the experimental error.

The obtained results point out that the presence of a sufficiently high fraction of anatase phase in the catalyst sample is necessary to have a significant increase in the photocatalytic activity. In fact, the samples TiO₂_0 h and TiO₂_2 h, having a phase composition of 15% anatase—85% brookite and 53% anatase—47% brookite, respectively, present a low photocatalytic activity, in spite of a very high SSA (503 and 354 m²/g, respectively). Surprisingly, the TiO₂_8 h sample shows a much lower photocatalytic activity (52%) than the TiO₂_16 h (72%) and TiO₂_24 h (68%) in spite of its higher SSA (350.0 vs. 336.5 and 255.7 m²/g, respectively). This evidence can be explained considering that, once the conversion to the anatase phase takes place, there are different properties of the TiO₂ samples that may play a role on their photocatalytic activity. A comparison of the characteristics and the photocatalytic efficiency of the TiO₂_8 h and TiO₂_16 h samples allows us to safely infer that the SSA is not essential in improving the catalytic activity, at least in a certain range. Indeed, SSA decreases as

duration of the thermal treatment increases, while the efficiency of the photocatalytic degradation of MB increases with the duration of the thermal treatment of the nanostructured catalyst assisting the decolouration process. It can be noticed that, concomitantly, pore width and volume remain almost unchanged, also upon prolonged thermal treatment. To further elucidate the photocatalytic behaviour of the material, FTIR spectroscopic investigation was carried out on the TiO₂ NP samples throughout the thermal treatment duration. Interestingly, for the three investigated TiO₂ samples (TiO₂_8 h, TiO₂_16 h and TiO₂_24 h; Figure S2), the intensity of the band associated with O–H stretching decreases for prolonged thermal treatment. Such evidence could be consistent with the fact that the amount of OH groups, that are at the surface of the TiO₂ NPs, and that basically derive from the synthetic conditions, being therefore randomly distributed inside and outside TiO₂ NP aggregates, decreases. Such OH groups can be thought to effectively react with the photogenerated holes in the nanocatalyst, thus leading to OH radicals. However, taking into account the size of the aggregates, the surface particles represent a fraction of the total; therefore, it is reasonable to assume that a large fraction of such OH groups is located inside the aggregate, and, thus, have a much lower probability to come in contact with MB and assist its degradation. Conversely, the OH groups located on the inner, less accessible surface of the photocatalyst, may serve rather as hole scavenger than to promote the photocatalytic process. Such an effect becomes evident once the evolution of the crystalline phase composition reached a plateau and the SSA decrease is not dramatic. Prolonging the thermal treatment, i.e., sample TiO₂_24 h, the intensity of the OH group band in FTIR spectra, and hence their overall amount in the whole sample, further decreases, while an increase in the anatase fraction occurs (81%), thus leading us to assume an overall increase in photocatalytic activity. On the contrary, MB photodegradation occurred to a lower, or at least comparable—considering the experimental error—extent ($68 \pm 5\%$ vs. $72 \pm 4\%$ for TiO₂_16 h). Such results could be accounted for by the strong decrease in SSA that drops to $255.7 \text{ m}^2/\text{g}$, with a loss in SSA of $81 \text{ m}^2/\text{g}$ with respect to TiO₂_16 h. It can be proposed that such a loss may counterbalance the increase in photocatalytic performances expected from the decrease in OH groups on the inner surface of the aggregate, thus finally resulting in a comparable photocatalytic activity.

Finally, a comparison of the photocatalytic performance of the TiO₂_16 h, thermally treated at 110° with that recorded for a sample prepared using the same preparative conditions, but introducing a calcination step at 450°C for 2 h [22] (referred to as TiO₂_450 °C in the following), shows that the former performs much better than the sample calcinated at 450°C , with a 1.5% increase in the photodegradation percentage (Figure 10).

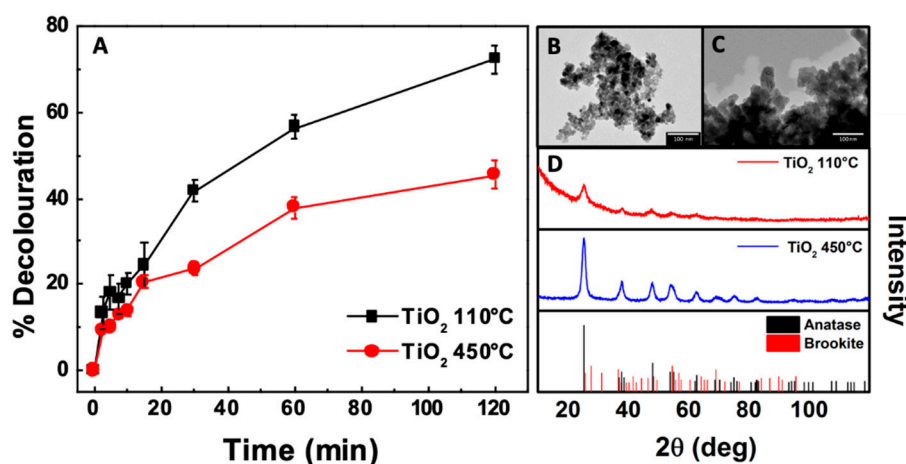


Figure 10. (A) TEM image of TiO₂ NPs calcined at 450°C and comparison with TiO₂_16 h (B). (C) XRD patterns of TiO₂_16 h and TiO₂_24 h. (D) Time course of the MB decolouration experiments under UV irradiation assisted by TiO₂ thermal treated at 110°C for 16 h (TiO₂_16 h sample) and TiO₂ calcinated for 2 h at 450°C (TiO₂_450 °C).

Such behaviour is particularly interesting when considering the crystal phase of the samples. Indeed, it looks like that the sample calcined at 450 °C, and due to the preparative conditions, it is entirely anatase in phase with a SSA of 69.1 m²/g [22], while the sample obtained after a low-temperature treatment presents a small fraction of brookite and a much higher SSA (336.5 m²/g). Therefore, the prevalence of the anatase phase does not appear to be a sufficiently decisive factor to explain alone the photocatalytic activity of the photocatalyst, but it is rather a specific combination of different structural, chemical and morphological characteristics that contribute to defining the photocatalytic behaviour [44,45]. Remarkably, this comparison highlights how a low-temperature procedure may be much more effective than a process carried out at high temperature, with an evident technological advantage in terms of requirements for the materials manufacturing. Finally, we performed additional experiments to compare the photocatalytic performance of our samples with that of TiO₂ P25, tested as a commercial benchmark. The results of the comparison, reported in the Supporting Information (Figures S3 and S4), point out that the decoloration extent for the reaction assisted by TiO₂ P25 (83 ± 5%) is slightly higher than that obtained when the TiO₂-16 h sample is used (72 ± 4%). However, a decisive assessment could not be safely performed, considering the different characteristics of the investigated photocatalyst with respect to the commercially available counterpart.

3. Materials and Methods

3.1. Materials

All chemicals were used as received without further purification. Titanylsulfate (TiOSO₄, 29% TiO₂, 17% H₂SO₄), ammonium bicarbonate (NH₄HCO₃ 99%), methylene blue (3,7-bis(dimethylamino)-phenazathionium chloride, MB) and all solvents were purchased from Aldrich Chemical reagent (Darmstadt, Germany). All solvents used were of analytical grade. MilliQ water was employed for preparation of all aqueous solutions.

3.2. Synthesis of TiO₂ Nanoparticles

The synthesis of TiO₂ nanoparticles (NPs) used of TiOSO₄ as TiO₂ precursor, that was selected due to its cost effectiveness, and exploited a simple precipitation method in alkaline aqueous solution. Briefly, 50 mL of 0.64 M TiOSO₄ solution were added dropwise in 76 mL of 2.00 M NH₄HCO₃ solution. After the complete mixing, the pH of the solution was adjusted to pH 8 by adding a proper amount of 2.00 M NH₄HCO₃. The obtained precipitate was repeatedly washed by subsequent cycles of dispersion in water and centrifugation at 3000 rpm. Afterwards, the product was thermally treated in oven at 110 °C to promote crystallization and to enhance the photocatalytic properties. A systematic study of the effect of the thermal treatment time was performed in the time range 2–24 h. The samples treated for 2–8–16–24 h were characterized by SEM, TEM, XRD, BET and photocatalytic experiments.

3.3. Catalyst Characterization

3.3.1. UV-Vis Absorbance Spectroscopy and Diffuse Reflectance Spectroscopy

UV-Vis absorption spectra and diffuse reflectance (DR) spectra were recorded with a UV-Vis-NIR Cary 5 (Agilent Technologies, Inc., Santa Clara, CA, USA) spectrophotometer. DR spectra were plotted in Kubelka-Munk (KM) arbitrary unit vs. wavelength. Band gap energy (E_g) was calculated by graphical extrapolation. Plotting a modified Kubelka-Munk function as a function of energy, the E_g was measured from the value of the intercept between the tangent of the curve and the axis on which the energies are reported [24].

3.3.2. FTIR Spectroscopy

Fourier transform infrared (FTIR) spectra of TiO₂ samples were recorded using a Perkin-Elmer Spectrum One spectrometer (Waltham, MA, USA) equipped with a deuterated tryglycine sulfate (DTGS)

detector. Spectra were collected with a resolution of 4 cm^{-1} operating in Attenuated Total Reflection (ATR) mode, using a three-bounce 4 mm-diameter diamond microprism as internal reflection element (SensIR technologies). Powders were cast directly onto the internal reflection element, carefully covering the upper face of the diamond crystal. The spectra for all experiments were collected with a resolution of 4 cm^{-1} in the range $2300\text{--}4000\text{ cm}^{-1}$.

3.3.3. Thermogravimetry

TGA experiments were carried out with a TGA/DSC1 STAR system (Mettler Toledo, Bristol, UK). The sample TiO_2 0 h T.T (10 mg) was fast heated from room temperature up to $110\text{ }^\circ\text{C}$ (heating ramp of $90\text{ }^\circ\text{C}/\text{min}$) under air flow ($30\text{ mL}/\text{min}$), then was treated under the same air flow at $110\text{ }^\circ\text{C}$ for 2 and 8 h, respectively, in order to monitor the weight loss and heat-flow occurring under the oven drying conditions used for the treatment of the TiO_2 samples.

3.3.4. Specific Surface Area and Pore Size Distribution

Specific surface area (SSA) and pore size distribution of the samples were determined by N_2 adsorption-desorption isotherms at $-196\text{ }^\circ\text{C}$ using ASAP 2020 Plus Micromeritics (Norcross, GA, USA). All the samples were pre-treated under vacuum at $80\text{ }^\circ\text{C}$ for 2 h prior to the measurements, except the sample labelled as TiO_2 0 h T.T, which was pre-treated under vacuum at $25\text{ }^\circ\text{C}$ for 2 h. The specific surface area was calculated using the Brunauer-Emmett-Teller (BET) method applied to the adsorption branch in the range $0.05\text{--}0.30\text{ p}/\text{p}_0$ [46]. The pore size distribution and cumulative pore volume vs. pore size were determined by comparing different methods, the Barrett-Joyner-Halenda (BJH) [47], the Gurvitsch [42] and the Horvath-Kavazoe methods [43]. The total pore volume of pores with sizes less than 50 nm was also estimated from single point desorption at p/p_0 equal to 0.98. The obtained textural parameters were quoted with a precision of $\pm 10\%$.

3.3.5. Transmission Electron Microscopy Investigation

Transmission electron microscopy (TEM) analysis was performed by means of a JEOL JEM-1011 (JEOL, Akishima, Tokyo, Japan) microscope operating at 100 kV. The TEM samples were prepared by casting a drop of TiO_2 methanol solution onto a carbon hollowed TEM grid. High-resolution transmission electron microscopy (HRTEM) imaging and STEM/EDS analyses (scanning transmission electron microscopy/energy dispersive spectroscopy) was carried out on a JEOL JEM-2200FS TEM (Schottky emitter), equipped with a CEOS C_5 corrector for the objective lens, and an in-column image filter (Ω -type), operated at 200 kV.

3.3.6. Scanning Electron Microscopy Investigation

Field emission scanning electron microscopy (FE-SEM) was performed by using a Zeiss Sigma microscope (Carl Zeiss Co., Oberkochen, Germany) operating in the range $0.5\text{--}20\text{ kV}$ and equipped with an in-lens secondary electron detector and an INCA Energy Dispersive Spectroscopy (EDS) detector. FE-SEM samples were prepared by casting a few drops of nanoparticle suspension in ethanol onto a silicon slide. Samples were mounted onto stainless-steel sample holders by using double-sided carbon tape and grounded by silver paste.

3.3.7. XRD Characterization

XRD patterns were recorded with a D8-Discover Bruker diffractometer (Bruker AXS GmbH, Karlsruhe, Germany) equipped with a Cu source (operated at $40/40\text{ mA}/\text{kV}$), a Goebel mirror, an Eulerian cradle goniometer, and a scintillator detector. The samples were prepared by depositing the sample from a concentrated colloidal dispersion onto a silicon substrate, and then allowing the solvent to evaporate. XRD patterns were collected, in 2θ scan mode with a fixed incident angle of 5° , moving the detector over the 2θ range $10^\circ\text{--}120^\circ$ with a step size of 0.05° .

The XRD patterns were analyzed by a whole-profile Rietveld based fitting program (FULLPROF) [48] to evaluate the crystalline domain apparent size at different heating time as reported in Table 2.

A quantitative phase analysis was also carried out to obtain the structural models of mixed compounds, by Rietveld method by using Quanto [49], a Rietveld program specialized for quantitative phase analysis (QPA) of polycrystalline mixtures.

3.3.8. Photocatalytic Experiments

The photocatalytic activity of the prepared TiO₂ samples was evaluated in an aqueous water suspension under UV light irradiation. ($\lambda = 254$ nm; light flux 0.2 mW/cm² determined by radiometer (Delta Ohm Data Logger) 9721), using an organic dye, methylene blue (MB) as a model target compound. The TiO₂ powder was suspended in a glass beaker containing a 10⁻⁵ M MB solution in milliQ water at pH 6. The pH value was carefully adjusted by the addition of HCl 0.1M and NaOH 0.1M. The MB-TiO₂ dispersion was left to stir in the dark for 30min to reach the adsorption-desorption equilibrium. Afterward, the suspension was irradiated under continuous stirring by a UV fluorescent lamp located at a distance of 6 cm over the beaker surface. At scheduled time intervals, aliquots were collected, purified by centrifugation, and the MB concentration was estimated by absorption spectroscopy as a function of reaction time. The percentage of decoloration as a function of reaction time was calculated using the following equation:

$$\% \text{ Decoloration} = [(A_0 - A_t)/A_0] \times 100 \quad (1)$$

As control experiments, the MB adsorption in the dark and the direct photolysis of MB, respectively, were investigated.

4. Conclusions

The decomposition of a cost effective precursor, TiOSO₄ in aqueous alkaline solution, at room temperature, followed just by a mild thermal treatment in oven (110 °C) has been established as a valuable synthetic approach able to supply mesoporous TiO₂ NPs in the gram-scale, without adding any templating, porogen agent. Optical (DRS), morphologic (TEM, SEM), physical chemical (TGA, DSC, BET) and structural (XRD, HRTEM) investigations demonstrated the possibility to tune the properties of the catalyst as a function of thermal treatment duration. The prepared nanostructured material was shown to be an effective photocatalyst able to assist in the UV-induced degradation of MB, the model compound selected for the photocatalytic test. The investigation has highlighted the strong interplay of the different characteristics, namely surface area, crystalline phase, and surface chemistry, of the prepared nanomaterials in defining their photocatalytic properties. Moreover, the comparison of photocatalytic behavior of two samples, prepared by using the same procedure, but then thermally treated in an oven at 110 °C and calcined at 450 °C, respectively, show the advantage of the mild treatment against the harsher calcination step. Overall, the presented results demonstrate that the proposed approach offers a facile and sustainable route to promptly access a photocatalyst, that may be used in technologically viable systems for the photocatalytic degradation of organic compounds, thus definitely representing a step forward toward the real application of TiO₂-based photocatalysis in the field of environmental depollution.

Supplementary Materials: The following are available online at <http://www.mdpi.com/2073-4344/10/8/893/s1>, Figure S1: Quantitative phase analysis performed by Quanto performed on the XRD patterns at (a) 2 h, (b) 4 h, (c) 8 h, (d) 16 h, (e) 24 h of thermal treatment, Figure S2: FTIR Spectra measured in ATR mode of TiO₂_0 h (orange line); TiO₂_8 h (red); TiO₂_16 h (blue); TiO₂_24 h (light blue) in the range 4000–2300 cm⁻¹, Figure S3: Time course evolution of Methylene Blue (MB) decolouration at pH 6, under UV assisted by TiO₂_16h (blue line), TiO₂_P25 (red line). Control experiments in dark condition are reported for TiO₂_16 h (black line) for TiO₂ P25 (violet line). Figure S4: Pictures of MB solution 10⁻⁵ M containing photocatalyst TiO₂ P25 (panel A) and TiO₂_16 h (panel B).

Author Contributions: Conceptualization M.D., F.P., A.T., M.L.C., R.C.; Formal analysis M.D., F.P., R.C., T.S., C.G., R.B., N.G., L.F.L., F.M.; Funding acquisition M.S., A.A., M.L.C., R.C.; Investigation M.D., F.P., A.T., T.S., C.G., R.B., N.G., L.F.L., F.M., R.C.; Supervision A.A., M.S., M.L.C., R.C.; Writing—original draft M.D., F.P., T.S., C.G., R.B., N.G., L.F.L., F.M., M.L.C., R.C.; Writing—review & editing F.P., L.F.L., M.L.C., R.C. All authors have read and agreed to the published version of the manuscript.

Funding: This work was partially supported by the Italian Apulia Region funded “FontanApulia” (WOBV6K5) and by the Italian PON MIUR “Energy for TARANTO” (Proposal Code ARS01_00637) projects.

Acknowledgments: The authors are grateful to National Interuniversity Consortium of Materials Science and Technology (INSTM).

Conflicts of Interest: The authors declare no conflict of interest.

References

1. Coenen, T.; Logist, F.; Van de Moortel, W.; Luyten, J.; Van Impe, J.; Degrève, J. Geometry optimization of photochemical reactors for advanced oxidation processes. In *Computer Aided Chemical Engineering*; Kraslawski, A., Turunen, I., Eds.; Elsevier: Amsterdam, The Netherlands, 2013; Volume 32, pp. 829–834.
2. Comninellis, C.; Kapalka, A.; Malato, S.; Parsons, S.A.; Poullos, I.; Mantzavinos, D. Advanced oxidation processes for water treatment: Advances and trends for R&D. *J. Chem. Technol. Biotechnol.* **2008**, *83*, 769–776. [[CrossRef](#)]
3. Ângelo, J.; Andrade, L.; Madeira, L.M.; Mendes, A. An overview of photocatalysis phenomena applied to NO_x abatement. *J. Environ. Manag.* **2013**, *129*, 522–539. [[CrossRef](#)] [[PubMed](#)]
4. Chong, M.N.; Jin, B.; Chow, C.W.K.; Saint, C. Recent developments in photocatalytic water treatment technology: A review. *Water Res.* **2010**, *44*, 2997–3027. [[CrossRef](#)]
5. Petronella, F.; Truppi, A.; Ingrosso, C.; Placido, T.; Striccoli, M.; Curri, M.L.; Agostiano, A.; Comparelli, R. Nanocomposite materials for photocatalytic degradation of pollutants. *Catal. Today* **2017**, *281*, 85–100. [[CrossRef](#)]
6. Yu, Z.; Gao, X.; Yao, Y.; Zhang, X.; Bian, G.-Q.; Wu, W.D.; Chen, X.D.; Li, W.; Selomulya, C.; Wu, Z.; et al. Scalable synthesis of wrinkled mesoporous titania microspheres with uniform large micron sizes for efficient removal of Cr(vi). *J. Mater. Chem. A* **2018**, *6*, 3954–3966. [[CrossRef](#)]
7. Gupta, S.; Tripathi, M. A review on the synthesis of TiO₂ nanoparticles by solution route. *Cent. Eur. J. Chem.* **2011**, *10*, 279–294. [[CrossRef](#)]
8. Petronella, F.; Truppi, A.; Dell’Edera, M.; Agostiano, A.; Curri, M.L.; Comparelli, R. Scalable synthesis of mesoporous TiO₂ for environmental photocatalytic applications. *Materials* **2019**, *12*, 1853. [[CrossRef](#)]
9. Kholmanov, I.N.; Barborini, E.; Vinati, S.; Piseri, P.; Podestà, A.; Ducati, C.; Lenardi, C.; Milani, P. The influence of the precursor clusters on the structural and morphological evolution of nanostructured TiO₂ under thermal annealing. *Nanotechnology* **2003**, *14*, 1168–1173. [[CrossRef](#)]
10. Malekshahi Byranvand, M.; Nemati Kharat, A.; Fatholahi, L.; Malekshahi Beiranvand, Z. A Review on Synthesis of Nano-TiO₂ via Different Methods. *J. Nanostruct.* **2013**, *3*, 1–9. [[CrossRef](#)]
11. Noman, M.T.; Ashraf, M.A.; Ali, A. Synthesis and applications of nano-TiO₂: A review. *Environ. Sci. Pollut. Res.* **2019**, *26*, 3262–3291. [[CrossRef](#)]
12. Augugliaro, V.; Palmisano, L.; Sclafani, A.; Minero, C.; Pelizzetti, E. Photocatalytic degradation of phenol in aqueous titanium dioxide dispersions. *Toxicol. Environ. Chem.* **1988**, *16*, 89–109. [[CrossRef](#)]
13. Radha, E.; Komaraiah, D.; Reddy, M.V.; Sayanna, R.; Sivakumar, J. Structural, optical and photocatalytic properties of anatase/rutile TiO₂ Nanoparticles. *i-manag. J. Mater. Sci.* **2019**, *6*, 43–49. [[CrossRef](#)]
14. Kawahara, T.; Ozawa, T.; Iwasaki, M.; Tada, H.; Ito, S. Photocatalytic activity of rutile–anatase coupled TiO₂ particles prepared by a dissolution–reprecipitation method. *J. Colloid Interface Sci.* **2003**, *267*, 377–381. [[CrossRef](#)]
15. Xu, H.; Li, G.; Zhu, G.; Zhu, K.; Jin, S. Enhanced photocatalytic degradation of rutile/anatase TiO₂ heterojunction nanoflowers. *Catal. Commun.* **2015**, *62*, 52–56. [[CrossRef](#)]
16. Kozhevnikova, N.S.; Ul’yanova, E.S.; Shalaeva, E.V.; Zamyatin, D.A.; Bokunyaeva, A.O.; Yushkov, A.A.; Kolosov, V.Y.; Buldakova, L.Y.; Yanchenko, M.Y.; Gorbunova, T.I.; et al. Low-temperature sol–gel synthesis and photoactivity of nanocrystalline TiO₂ with the anatase/brookite structure and an amorphous component. *Kinet. Catal.* **2019**, *60*, 325–336. [[CrossRef](#)]

17. Preethi, L.K.; Mathews, T. Electrochemical tuning of heterojunctions in TiO₂ nanotubes for efficient solar water splitting. *Catal. Sci. Technol.* **2019**, *9*, 5425–5432. [[CrossRef](#)]
18. Zhao, H.; Liu, L.; Andino, J.M.; Li, Y. Bicrystalline TiO₂ with controllable anatase–brookite phase content for enhanced CO₂ photoreduction to fuels. *J. Mater. Chem. A* **2013**, *1*, 8209–8216. [[CrossRef](#)]
19. Santhosh, N.; Govindaraj, R.; Senthil Pandian, M.; Ramasamy, P.; Mukhopadhyay, S. Mesoporous TiO₂ microspheres synthesized via a facile hydrothermal method for dye sensitized solar cell applications. *J. Porous Mater.* **2016**, *23*, 1483–1487. [[CrossRef](#)]
20. Hernández-Gordillo, A.; Camperoa, A.; Vera-Robles, L.I. Mesoporous TiO₂ synthesis using a semi-hard biological template. *Micropor. Mesopor. Mater.* **2018**, *270*, 140–148. [[CrossRef](#)]
21. Madras, G.; McCoy, B.J. Kinetic model for transformation from nanosized amorphous TiO₂ to anatase. *Cryst. Growth Des.* **2007**, *7*, 250–253. [[CrossRef](#)]
22. Truppi, A.; Petronella, F.; Placido, T.; Margiotta, V.; Lasorella, G.; Giotta, L.; Giannini, C.; Sibillano, T.; Murgolo, S.; Mascolo, G.; et al. Gram-scale synthesis of UV–vis light active plasmonic photocatalytic nanocomposite based on TiO₂/Au nanorods for degradation of pollutants in water. *Appl. Catal. B* **2019**, *243*, 604–613. [[CrossRef](#)]
23. Comparelli, R. Special issue: Application of photoactive nanomaterials in degradation of pollutants. *Materials* **2019**, *12*, 2459. [[CrossRef](#)] [[PubMed](#)]
24. López, R.; Gómez, R. Band-gap energy estimation from diffuse reflectance measurements on sol–gel and commercial TiO₂: A comparative study. *J. Sol-Gel Sci. Technol.* **2012**, *61*, 1–7. [[CrossRef](#)]
25. Carlucci, C.; Xu, H.; Scremin, B.F.; Giannini, C.; Altamura, D.; Carlino, E.; Videtta, V.; Conciauro, F.; Gigli, G.; Ciccarella, G. Selective synthesis of TiO₂ nanocrystals with morphology control with the microwave-solvothermal method. *CrystEngComm* **2014**, *16*, 1817–1824. [[CrossRef](#)]
26. Gopalakrishnamurthy, H.S.; Subba Rao, M.; Narayanan Kutty, T.R. Thermal decomposition of titanyl oxalates IV. Strontium and calcium titanyl oxalates. *Thermochim. Acta* **1975**, *13*, 183–191. [[CrossRef](#)]
27. Mino, L.; Cesano, F.; Scarano, D.; Spoto, G.; Martra, G. Molecules and heterostructures at TiO₂ surface: The cases of H₂O, CO₂, and organic and inorganic sensitizers. *Res. Chem. Intermed.* **2019**, *45*, 5801–5829. [[CrossRef](#)]
28. Dambournet, D.; Belharouak, I.; Amine, K. Tailored preparation methods of tio₂ anatase, rutile, brookite: Mechanism of formation and electrochemical properties. *Chem. Mater.* **2010**, *22*, 1173–1179. [[CrossRef](#)]
29. Kobayashi, M.; Petrykin, V.; Tomita, K.; Kakihana, M. Hydrothermal synthesis of brookite-type titanium dioxide with snowflake-like nanostructures using a water-soluble citratoperoxotitanate complex. *J. Cryst. Growth* **2011**, *337*, 30–37. [[CrossRef](#)]
30. Kandiel, T.A.; Feldhoff, A.; Robben, L.; Dillert, R.; Bahnemann, D.W. Tailored titanium dioxide nanomaterials: Anatase nanoparticles and brookite nanorods as highly active photocatalysts. *Chem. Mater.* **2010**, *22*, 2050–2060. [[CrossRef](#)]
31. Shi, L.; Weng, D. Highly active mixed-phase TiO₂ photocatalysts fabricated at low temperature and the correlation between phase composition and photocatalytic activity. *J. Environ. Sci.* **2008**, *20*, 1263–1267. [[CrossRef](#)]
32. Qi, K.; Xin, J.H. Room-temperature synthesis of single-phase anatase TiO₂ by aging and its self-cleaning properties. *ACS Appl. Mater. Interfaces* **2010**, *2*, 3479–3485. [[CrossRef](#)] [[PubMed](#)]
33. Chuang, H.-Y.; Chen, D.-H. Catalyst-free low temperature synthesis of discrete anatase titanium dioxide nanocrystals with highly thermal stability and UVC-cut capability. *J. Nanopart. Res.* **2008**, *10*, 233–241. [[CrossRef](#)]
34. Zhang, P.; Yin, S.; Sato, T. A low-temperature process to synthesize rutile phase TiO₂ and mixed phase TiO₂ composites. *Mater. Res. Bull.* **2010**, *45*, 275–278. [[CrossRef](#)]
35. Di Paola, A.; Bellardita, M.; Palmisano, L. Brookite, the least known TiO₂ photocatalyst. *Catalysts* **2013**, *3*, 36–73. [[CrossRef](#)]
36. Chen, X.; Mao, S.S. Titanium dioxide nanomaterials: Synthesis, properties, modifications, and applications. *Chemical Rev.* **2007**, *107*, 2891–2959. [[CrossRef](#)] [[PubMed](#)]
37. Sing, K.S.W.; Williams, R.T. Physisorption hysteresis loops and the characterization of nanoporous materials. *Adsorpt. Sci. Technol.* **2004**, *22*, 773–782. [[CrossRef](#)]
38. Zhang, H.; Banfield, J.F. Understanding polymorphic phase transformation behavior during growth of nanocrystalline aggregates: Insights from TiO₂. *J. Phys. Chem. B* **2000**, *104*, 3481–3487. [[CrossRef](#)]

39. Tanev, P.T.; Vlaev, L.T. An attempt at a more precise evaluation of the approach to mesopore size distribution calculations depending on the degree of pore blocking. *J. Colloid Interface Sci.* **1993**, *160*, 110–116. [[CrossRef](#)]
40. Zhang, R.; Elzatahry, A.A.; Al-Deyab, S.S.; Zhao, D. Mesoporous titania: From synthesis to application. *Nano Today* **2012**, *7*, 344–366. [[CrossRef](#)]
41. Niu, B.; Wang, X.; Wu, K.; He, X.; Zhang, R. Mesoporous titanium dioxide: Synthesis and applications in photocatalysis, energy and biology. *Materials* **2018**, *11*, 1910. [[CrossRef](#)]
42. Lukens, W.W.; Schmidt-Winkel, P.; Zhao, D.; Feng, J.; Stucky, G.D. Evaluating pore sizes in mesoporous materials: A simplified standard adsorption method and a simplified Broekhoff–de Boer method. *Langmuir* **1999**, *15*, 5403–5409. [[CrossRef](#)]
43. Horvath, G.; Kawazoe, K. Method for the calculation of effective pore size distribution in molecular sieve carbon. *J. Chem. Eng. Jpn.* **1983**, *16*, 470–475. [[CrossRef](#)]
44. Allen, N.S.; Mahdjoub, N.; Vishnyakov, V.; Kelly, P.J.; Kriek, R.J. The effect of crystalline phase (anatase, brookite and rutile) and size on the photocatalytic activity of calcined polymorphic titanium dioxide (TiO₂). *Polym. Degrad. Stab.* **2018**, *150*, 31–36. [[CrossRef](#)]
45. Matsukawa, Y.; Hirata, S.; Inada, M.; Enomoto, N.; Hojo, J.; Hayashi, K. Kinetic effects of polymorphs and surface areas on adsorption and photocatalytic decomposition of acetaldehyde on titania. *Chem. Eng. J.* **2020**, *397*, 125422. [[CrossRef](#)]
46. Brunauer, S.; Emmett, P.H.; Teller, E. Adsorption of Gases in Multimolecular Layers. *J. Am. Chem. Soc.* **1938**, *60*, 309–319. [[CrossRef](#)]
47. Barrett, E.P.; Joyner, L.G.; Halenda, P.P. The Determination of Pore Volume and Area Distributions in Porous Substances. I. Computations from Nitrogen Isotherms. *J. Am. Chem. Soc.* **1951**, *73*, 373–380. [[CrossRef](#)]
48. Rodriguez-Carvajal, J. Recent advances in magnetic structure determination by neutron powder diffraction. *Phys. B* **1993**, *192*, 55–69. [[CrossRef](#)]
49. Altomare, A.; Burla, M.C.; Giacovazzo, C.; Guagliardi, A.; Moliterni, A.G.G.; Polidori, G.; Rizzi, R. Quanto: A Rietveld program for quantitative phase analysis of polycrystalline mixtures. *J. Appl. Crystallogr.* **2001**, *34*, 392–397. [[CrossRef](#)]



© 2020 by the authors. Licensee MDPI, Basel, Switzerland. This article is an open access article distributed under the terms and conditions of the Creative Commons Attribution (CC BY) license (<http://creativecommons.org/licenses/by/4.0/>).